



Poleward migration of western North Pacific tropical cyclones driven by genesis location shift under global warming in HighResMIP-PRIMAVERA models



Mingyu Li¹, Chaoxia Yuan^{1,2}✉, Jiuwei Zhao¹ & Qingqing Li¹

The latitudinal position of lifetime maximum intensity (φ_{LMI}) of tropical cyclones (TCs) in the western North Pacific (WNP) has been observed to migrate poleward over the last several decades, but the cause remains not fully understood. In this study, we utilized 20 models from the PRIMAVERA project with different configurations to investigate long-term changes in the φ_{LMI} in the WNP. Over a hundred-year simulations under global warming, most models demonstrate a poleward shift of φ_{LMI} with a multi-model-mean rate of $0.068^\circ \text{ decade}^{-1}$. This poleward trend can be predominantly explained by the poleward shift of TC genesis latitude. Specifically, the poleward shift of TC genesis latitude contributes $0.28^\circ \text{ decade}^{-1}$ to the trend, the meridional shift of the Hadley circulation's ascending branch contributes $0.03^\circ \text{ decade}^{-1}$, but they are largely offset by the negative contribution of $-0.24^\circ \text{ decade}^{-1}$ by the decreasing lifetime maximum intensity.

Tropical cyclones (TCs) originate and intensify over warm tropical waters, posing significant threats to life and property upon landfall due to their destructive wind and extreme precipitation^{1–3}. Understanding long-term changes in TCs is crucial for developing effective mitigation and adaptation strategies. Kossin et al.^{4–6} revealed a notable poleward migration trend in the latitude at which TCs reach their lifetime maximum intensity (φ_{LMI}). This trend is particularly pronounced in the western North Pacific (WNP), the most active TC basin, which predominantly contributes to the poleward migration observed in the northern hemisphere. Projections indicate that this poleward migration is likely to continue into the 21st century, potentially increasing the TC exposure in parts of eastern China, Korea, and Japan^{4,6–9}.

The poleward migration of φ_{LMI} has been attributed to several factors^{10–17}. Some study emphasizes the genesis latitude shift as the primary driver^{12,14,16}. Sharmila and Walsh¹⁰ revealed that the shift in the regional Hadley circulation contributes to the poleward migration under global warming. Complementing the perspectives, Wang and Wu¹⁵ identified large-scale steering flow adjustments as the dominant control on the historical trend in φ_{LMI} . In addition, Feng et al.¹³ suggested that seasonally non-uniform large-scale environmental changes drive the poleward migration of φ_{LMI} through intensified Pacific Walker Circulation, which is further evidenced in the subsequent research¹⁷. Although the φ_{LMI} is relatively robust to

heterogeneities in best-track data caused by temporal inconsistencies in data quality^{5,11}, marked differences in the φ_{LMI} migration rates in the WNP have been reported^{4,11,18}. These discrepancies are likely due to different periods selected for the trend studies^{11,19,20}, as TC activities can be substantially influenced by decadal-to-multidecadal climate modes¹⁹ such as the Interdecadal Pacific Oscillation (IPO)^{21–23} and the Atlantic Multidecadal Oscillation (AMO)^{24–26}. Notably, after 1999, the φ_{LMI} exhibits an equatorward migration^{6,18,27}, highlighting cyclical oscillations superimposed on the secular long-term trend²⁸.

As mentioned above, the causality of the observed poleward migration of φ_{LMI} in the WNP in recent decades is controversial. The short observational history limits the reliability of studies on long-term changes in TC activities. Consequently, many researchers turn to numerical modeling as an alternative²⁹. However, TC simulations in numerical models are highly impacted by model configurations, such as horizontal resolution and air-sea coupling^{29–32}. It is thus of great interest to examine whether there is consensus on the poleward migration of φ_{LMI} among different models and whether the model setups, such as air-sea coupling, have consistent influences on the φ_{LMI} . To resolve the genesis-vs-track controversy^{14,15} and disentangle forced responses from multidecadal internal variations^{28,33}, a unified attribution framework across model hierarchies is imperative.

¹ State Key Laboratory of Climate System Prediction and Risk Management/Key Laboratory of Meteorological Disaster, Ministry of Education/Collaborative Innovation Center on Forecast and Evaluation of Meteorological Disasters, Nanjing University of Information Science and Technology, Nanjing, China. ²School of Artificial Intelligence, Nanjing University of Information Science and Technology, Nanjing, China. ✉e-mail: chaoxia.yuan@nuist.edu.cn

The European Union Horizon 2020s PProcess-based climate sIMulation: AdVances in high-resolution modelling and European climate Risk Assessment (PRIMAVERA) project provides an excellent opportunity^{34–37}. The project, which is also part of the CMIP6 High-Resolution Model Intercomparison Project (HighResMIP)³⁸, utilizes global models running in both atmospheric-only and air-sea coupled configurations at standard and higher resolutions to enhance our understanding of high-impact weather events³⁹. It offers a unique opportunity to explore the long-term changes in the φ_{LMI} in the WNP under global warming and to investigate possible impacts of model configuration on the φ_{LMI} . Here, we adopt both the relatively low (LR) and high-resolution (HR) atmospheric-only models (AGCMs) and their corresponding coupled models (CGCMs) from five modeling groups participating in the HighResMIP-PRIMAVERA project: CMCC-CM2⁴⁰, CNRN-CM6-1⁴¹, HadGEM3-GC31⁴², EC-Earth3P⁴³ and MPI-ESM1.2⁴⁴ (Supplementary Table 1). The reproducibility of φ_{LMI} including its spatial distributions and influential factors in these models during 1984–2014 is assessed. The long-term trends of φ_{LMI} during 1950–2050 are then examined, and possible drivers are investigated. Furthermore, differences between the ten pairs of AGCMs vs. CGCMs are compared to reveal the impacts of air-sea coupling on φ_{LMI} (see “Methods”).

Results

Model performance in simulating φ_{LMI}

The Taylor diagrams of the model simulations and observations for the spatial pattern of TC LMI during 1984–2014 are shown in Fig. 1. It is apparent that almost all models have pattern correlation coefficients (PCCs)

between 0.70 and 0.95, indicating that the models performance well in simulating the observed spatial pattern of TC LMI during 1984–2014. The normalized standard deviation mainly ranges from 1 to 2, indicating that the simulated spatial variation is larger than the observed. These standard deviations are less pronounced in the AGCMs (Fig. 1a) compared to their corresponding CGCMs (Fig. 1b). Further, the AGCMs predominantly exhibit RMSE values clustered within 0.5–1.0, while the CGCMs show a broader spread, with most RMSE values exceeding 1.0 and reaching up to 1.5. The multi-model ensemble mean (MME) PCC of all ten AGCMs is 0.85, which is 4% higher than that of CGCMs at 0.82; the MME RMSE of all ten AGCMs is 1.23, which is 13% lower than that of CGCMs at 1.42. The superior performance of AGCMs over CGCMs during 1984–2014 is likely due to the accurate boundary forcing provided by the prescribed observed SSTs.

Factors influencing φ_{LMI}

Although many factors can influence φ_{LMI} as mentioned above, the extent to which each factor affects φ_{LMI} remains unclear. Here, the relationship between the φ_{LMI} and the LMI itself is first examined. The observed φ_{LMI} and LMI exhibit a parabolic relationship (Fig. 2a, b). When the LMI is below/above Category 1 of the Saffir-Simpson scale (32–42 m s⁻¹), the φ_{LMI} moves poleward/equatorward, almost linearly with the increasing LMI. This is likely because weak TCs (below Category 1) tend to have longer lifespans if they become stronger, increasing their chances of moving further northward. Conversely, strong TCs (above Category 1) tend to stay over the warm oceans closer to the equator to achieve higher intensities. The observed

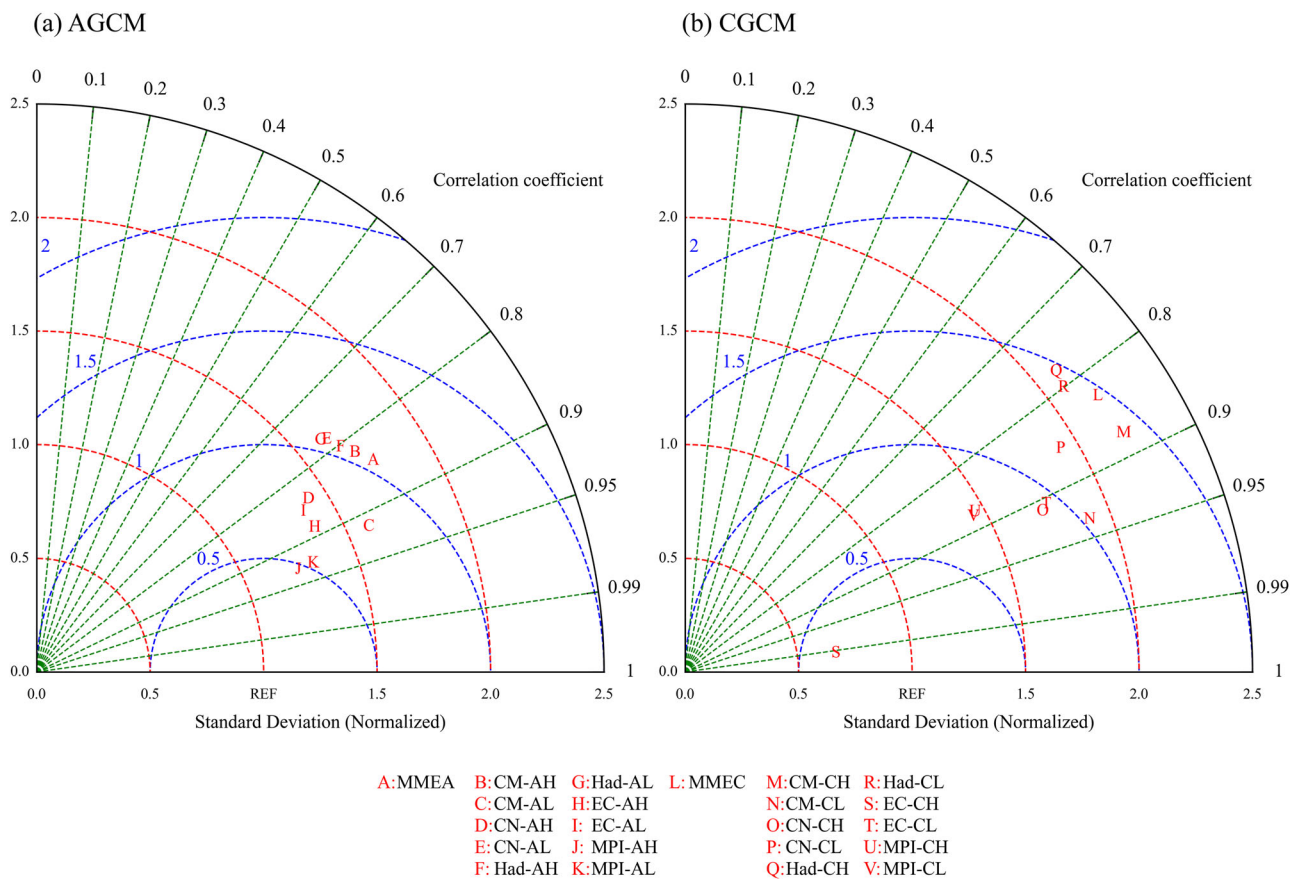


Fig. 1 | Taylor diagrams of model simulations and observations for the spatial pattern of TC LMI in the WNP over 1984–2014. a AGCMs and **b** CGCMs at HR and LR versions. The MME, HR, and LR versions are marked by different letters. The green radial lines represent the spatial correlation coefficient (PCC) between model simulations and observed data, with values ranging from 0 to 1. Higher PCC values indicate a stronger correlation. The blue dashed lines correspond to the Root Mean

Square Error (RMSE), which quantifies the differences between model simulations and observed data. Smaller RMSE values reflect improved model accuracy. The red dashed lines represent the standard deviation, indicating the variability of model simulations relative to the observed data. Larger standard deviations suggest greater variability in the model’s simulations.

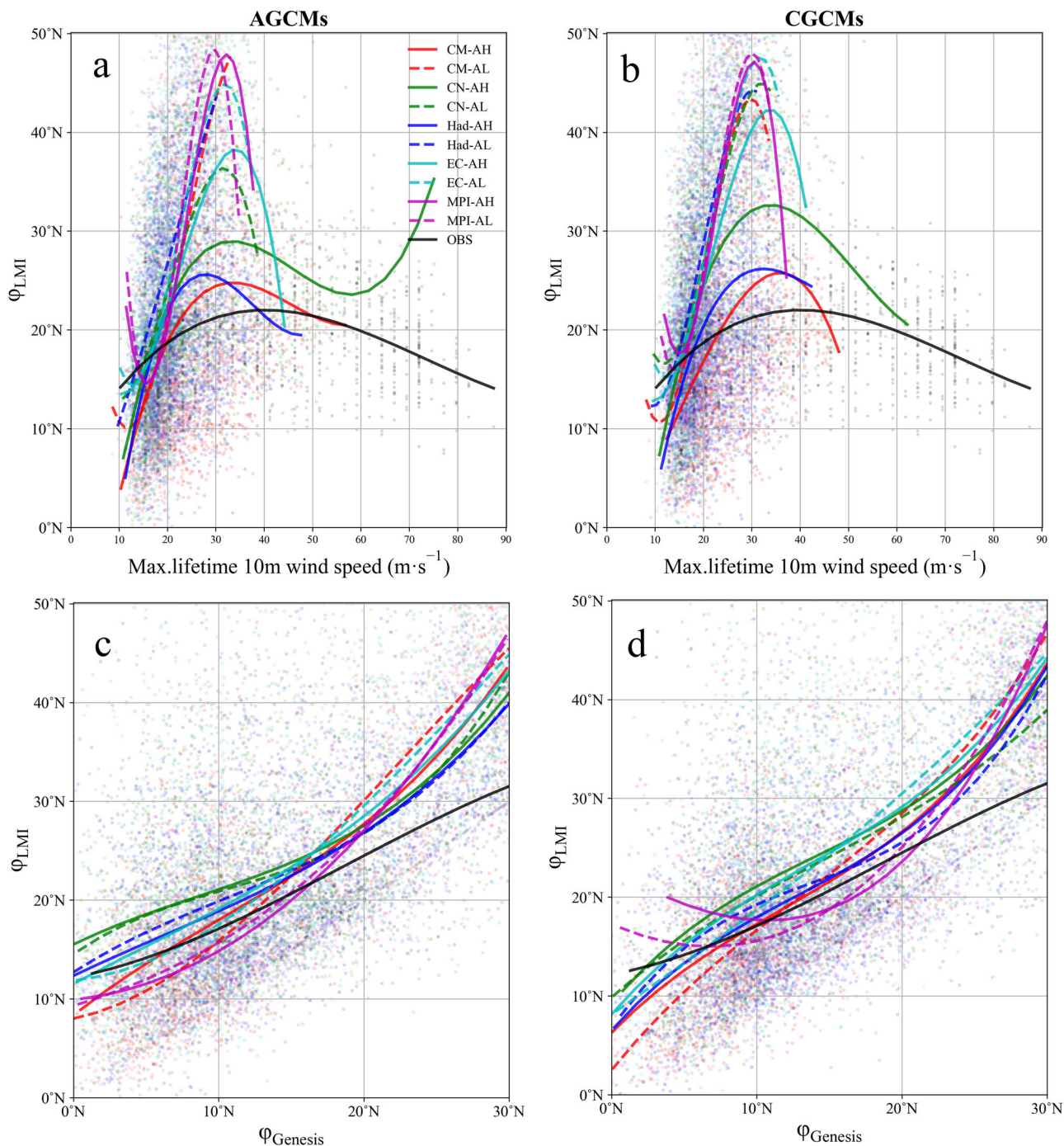


Fig. 2 | Relationships of ϕ_{LMI} with LMI and genesis latitude in observations and HighResMIP models. Scatter plots of **a**, **b** ϕ_{LMI} vs. LMI ($m s^{-1}$) and **c**, **d** ϕ_{LMI} vs. genesis latitude ($\phi_{Genesis}$) for all TCs during 1984–2014 based on the observations (dark dots) and numerical simulations (color dots) by **a**, **c** AGCMs and **b**, **d** CGCMs. Red dots represent CMCC-CM2, green dots represent CNRM-CM6-1, blue dots

represent HadGEM3-GC31, cyan dots represent EC-Earth3P and purple dots represent MPI-ESM1.2. The best-fit curves for each model with their 95% two-sided confidence intervals (shading) are interpolated. The solid and dashed lines represent HR and LR models, respectively.

parabolic relationship can be better simulated by the HR than the LR models simply because the HR models are capable of simulating intense TCs. The CN-AH is the only AGCM that can simulate TCs stronger than Category 3. However, these simulated Category-3 and even stronger TCs move unrealistically poleward compared to the observed, probably due to faster translation speeds of TCs in the middle latitudes in the models^{41,45}. On the other hand, incorporating air-sea coupling generally decreases the LMI of TCs (Fig. 2a, b). For example, Category 4 and further stronger TCs disappear in CN-CH, eliminating the unrealistic poleward displacement of the

corresponding ϕ_{LMI} (Fig. 2b). We note that both the AGCMs and CGCMs tend to simulate more frequent occurrences of weak TCs, and their ϕ_{LMI} has a much broader meridional extent than the observed (Fig. 2a, b).

The genesis latitudes of TCs are closely related to their ϕ_{LMI} ^{11,12}. They exhibit nearly linear relationships in both the observations and model simulations (Fig. 2c, d). It is reasonable that TCs forming at higher latitudes tend to achieve higher ϕ_{LMI} . However, biases still exist: simulated TCs tend to reach higher ϕ_{LMI} when they form at 15°N or further northward compared to the observations (Fig. 2d), while those forming near the equator

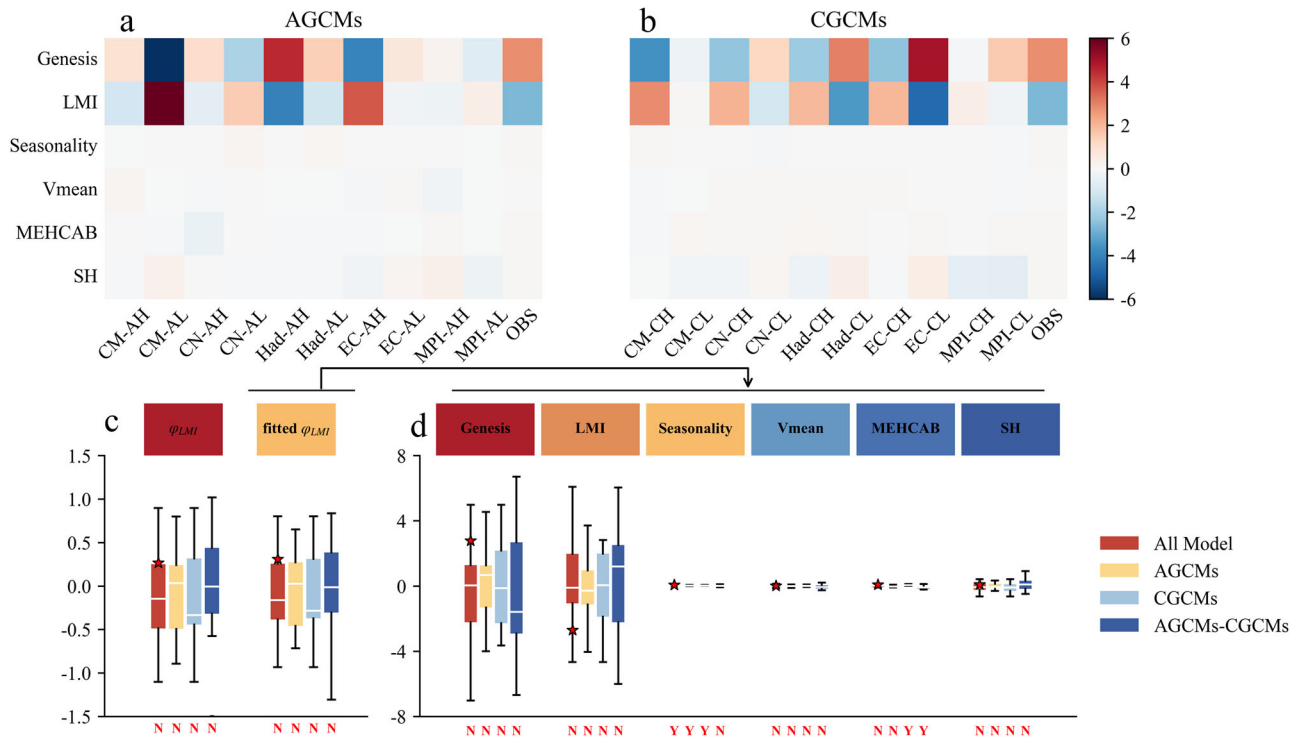


Fig. 3 | Contributions of six factors to the fitted trends. Heatmap of the contributions of the six factors to the fitted trends during 1984–2014 based on the **a** AGCMs and **b** CGCMs at their HR and LR configurations. **c** Boxplots of real and fitted trends (degree decade⁻¹) in the annual-mean φ_{LMI} during 1984–2014 for (red) all 20 models, (yellow) AGCMs, (light blue) CGCMs and the differences (dark blue) between the AGCMs vs. CGCMs. **d** The fitted trends can be decomposed to contributions by six influential factors, including the TC genesis latitude (Genesis), LMI, seasonality, meridional steering flow (Vmean), Meridional extent of Hadley circulation’s ascending branch (MEHCAB) and the WNPSH strength (SH), respectively.

The real and fitted trends and the contributions by the six factors based on the observations are interpolated as the red stars in (c, d). The bottom and top edges of each box denote the 25th and 75th percentiles, and the horizontal line (white) inside the box is the median. The bottom and top whiskers extend to the minimum and maximum within a distance of 1.5 times of the interquartile, and the outliers (outside the whiskers) are plotted with open circles. The letters “Y” and “N” beneath the horizontal axis in (c, d) indicate that over and less than 75% members show the same-signed values, respectively.

tend to have lower φ_{LMI} , particularly in the coupled models (Fig. 2d). This is consistent with the broader meridional range of φ_{LMI} in the models than in the observations as mentioned above. Nevertheless, both the AGCMs and CGCMs reproduce reasonably well the observed relationship between the TC genesis latitude and the φ_{LMI} .

In addition to the genesis latitude and LMI, other factors such as TC seasonality, meridional extent of Hadley circulation’s ascending branch (MEHCAB), meridional steering flow and the strength of WNP subtropical high (WNPSH) may also influence φ_{LMI} ^{10,13,46,47}. To compare their relative importance on φ_{LMI} , the indices of the six factors, including genesis latitude, LMI, TC seasonality, MEHCAB, meridional steering flow and WNPSH strength, are normalized and used to construct a multiple linear regression equation for the year-to-year variations in the annual-mean φ_{LMI} in the WNP during 1984–2014 (see “Methods”). The coefficient of each factor can also be regarded as the weight of its trend on the trend of annual-mean φ_{LMI} . This assumes that each factor influences the year-to-year variations of the annual-mean φ_{LMI} in the same manner as it impacts the long-term trend of the annual-mean φ_{LMI} . The coefficient and trend of each factor, the real and the fitted linear trends of annual-mean φ_{LMI} and the respective contributions by the six factors during 1984–2014 based on the observations and model simulations are provided in Fig. 3a, b and Supplementary Tables 2–4. It is evident that in the observations, the year-to-year variations in the annual-mean φ_{LMI} are primarily controlled by the genesis latitude and LMI, as their coefficients are the largest and statistically significant in the regression equation. Moreover, the fitted linear trend closely matches the real one in terms of sign and amplitude; both of them show poleward migration at a rate around 0.3° decade⁻¹. The trend in the genesis latitude predominantly contributes to the fitted trend. The trends in the MEHCAB

and WNPSH strength also play significant roles in the observed poleward migration. Conversely, the trend of LMI is opposite to the trend of genesis latitude and the fitted trend. On the other hand, the TC seasonality and meridional steering flow neither have significant relationships with the year-to-year variations of annual-mean φ_{LMI} , nor show large linear trends in the period of our interest. Therefore, their contribution to the poleward migration of annual-mean φ_{LMI} is limited (Fig. 3d and Supplementary Tables 2–4).

Similar to the observations, the genesis latitude and LMI are the two leading factors showing significant positive relationships with the year-to-year variations in the annual-mean φ_{LMI} in the historical simulations of all models during 1984–2014 (Supplementary Table 2). Specifically, the influence of genesis latitude on the interannual variations in the annual-mean φ_{LMI} is the largest with a multi-model-mean (MME) coefficient of 6.35. The influence of LMI plays a secondary role with an MME coefficient of 3.54. In contrast, eight/twelve models show positive/negative influences of TC seasonality on the annual-mean φ_{LMI} variations, among which four/no models show statistically significant influences. Five/fifteen models show positive/negative influences of MEHCAB on the year-to-year variations in the annual-mean φ_{LMI} , among which four/eleven models show statistically significant influences. Twelve/eight models show positive/negative influences of meridional steering flow on the annual-mean φ_{LMI} variations, among which eight/six models show statistically significant influences. Nine/eleven models exhibit positive/negative influences of WNPSH strength on the annual-mean φ_{LMI} variations, among which seven/six models show statistically significant influences. Therefore, the consensus among all 20 models is the significant positive impacts of the genesis latitude and LMI on the interannual variations in the annual-mean φ_{LMI} , with the

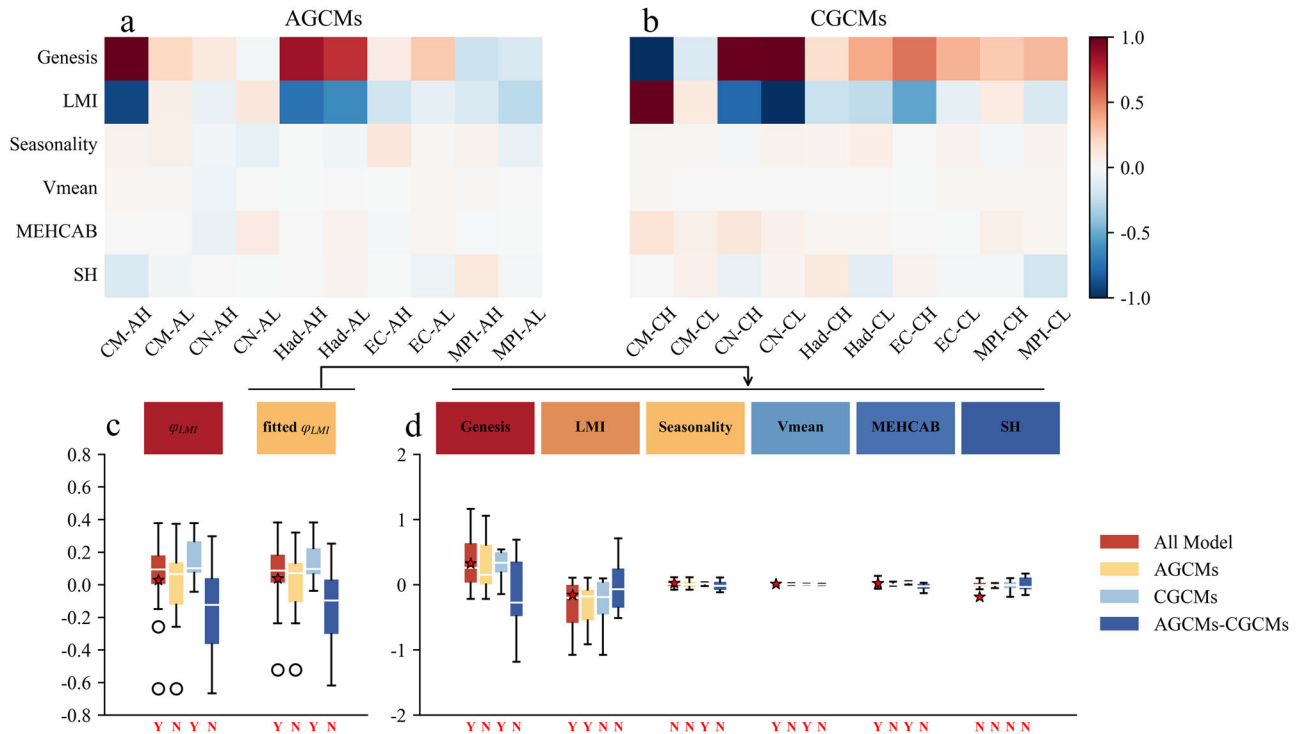


Fig. 4 | Contributions of six factors to the fitted trends. Similar to Fig. 3, but for the period of 1950–2050. Heatmap of the contributions of the six factors to the fitted trends based on the **a** AGCMs and **b** CGCMs at their HR and LR configurations. **c** Boxplots of real and fitted trends (degree decade⁻¹) for (red) all 20 models, (yellow) AGCMs, (light blue) CGCMs and the differences (dark blue) between the AGCMs

vs. CGCMs. **d** The fitted trends can be decomposed to contributions by six influential factors including the TC genesis latitude (Genesis), LMI, seasonality, meridional steering flow (Vmean), Meridional extent of Hadley circulation’s ascending branch (MEHCAB) and the WNPSH strength (SH), respectively.

former being more influential than the latter. For the other four factors, their importance to the interannual variations of the annual-mean φ_{LMI} is model-dependent. Even for subgroups such as the AGCMs and CGCMs, there is still no consensus regarding the influences of these four factors.

The fitted long-term trend by the six factors in each model is very close to the real trend directly calculated from the annual-mean φ_{LMI} (Fig. 3c and Supplementary Table 4). This reassures the feasibility of our method to attribute the trend. Similar to the observations, the genesis latitude and LMI have much larger coefficients than the other four factors, and contribute dominantly to the trends of annual-mean φ_{LMI} in each model (Fig. 3d and Supplementary Table 2). However, the trends of genesis latitude themselves are very diverse in both signs and amplitudes; ten models show negative trends, whereas the other ten models show positive trends (Supplementary Table 3). They have the opposite signs compared to the trends of LMI in all models. This indicates that if the genesis latitude of TC moves poleward, its LMI is expected to decrease. This is reasonable as the LMI is closely related to the large-scale environmental conditions, such as sea surface temperatures and mid-tropospheric humidity, that are more favorable for TC intensification near the equator^{19,48}. Additionally, Walsh et al.⁴⁹ have also pointed out that LMI in the WNP has shown a decreasing trend in recent years. Even though the trends of genesis latitude and LMI are opposite, the influence of genesis latitude on the trend of annual-mean φ_{LMI} is generally larger than LMI; the averaged contribution of genesis latitude in the 20 models is 1.25 times larger than that of LMI. Consequently, in almost all models (19 out of 20), the trend sign of annual-mean φ_{LMI} is the same as that of the genesis latitude. However, there is no consensus on the trend sign of genesis latitude itself, neither in the 20 models nor in their subgroups such as the AGCMs and CGCMs, which explains the diverse trends of annual-mean φ_{LMI} in the models. This also suggests that during 1984–2014, global warming may play a role in the changes of genesis latitude and thus annual-mean φ_{LMI} , but these influences are not predominant and may be surpassed by other low-frequency climate modes such as IPO and AMO^{21,23,25,26}, requiring longer-

term data to quantify the global-warming-induced response. Also, we note that the contribution of the other four factors to the trend of annual-mean φ_{LMI} is very small and negligible; the averaged contribution of genesis latitude on the trend of annual-mean φ_{LMI} is about 11/60/25/5 times larger than that of TC seasonality/meridional steering flow/MEHCAB/WNPSH strength (Fig. 3d and Supplementary Table 4).

Trends in the annual-mean φ_{LMI} during 1950–2050

Since the 31-year period from 1984 to 2014 is insufficient to largely eliminate the impacts of the decadal-to-multidecadal oscillations such as IPO and AMO on the trend of annual-mean φ_{LMI} , we utilized much longer-period simulations spanning 1950–2050 under the RCP5-8.5 scenario for the AGCMs or the SSP5-8.5 scenario for the CGCMs by the same 20 models to investigate the 101-year trend of annual-mean φ_{LMI} . As detailed in Fig. 4 and Supplementary Tables 8–10, in these 101-year simulations, the genesis latitude and LMI remain as the two dominant factors significantly positively influencing the year-to-year variations in the annual-mean φ_{LMI} . The influence of genesis latitude is greater than that of LMI, with the MME coefficient of genesis latitude at 7.49, 1.6 times larger than that of LMI at 4.76. Similar to the period of 1984–2014, the influences of the other four factors on the annual-mean φ_{LMI} are model-dependent. Fourteen/six models show positive/negative influences of TC seasonality on the year-to-year variations in the annual-mean φ_{LMI} , among which five/three models show statistically significant influences. Nine/eleven models show positive/negative influences of meridional steering flow on the year-to-year variations in the annual-mean φ_{LMI} , among which three/three models show statistically significant influences. Three/seventeen models show positive/negative influences of MEHCAB on the year-to-year variations in the annual-mean φ_{LMI} , among which two/twelve models show statistically significant influences. Finally, nine/eleven models show positive/negative influences of WNPSH strength on the year-to-year variations

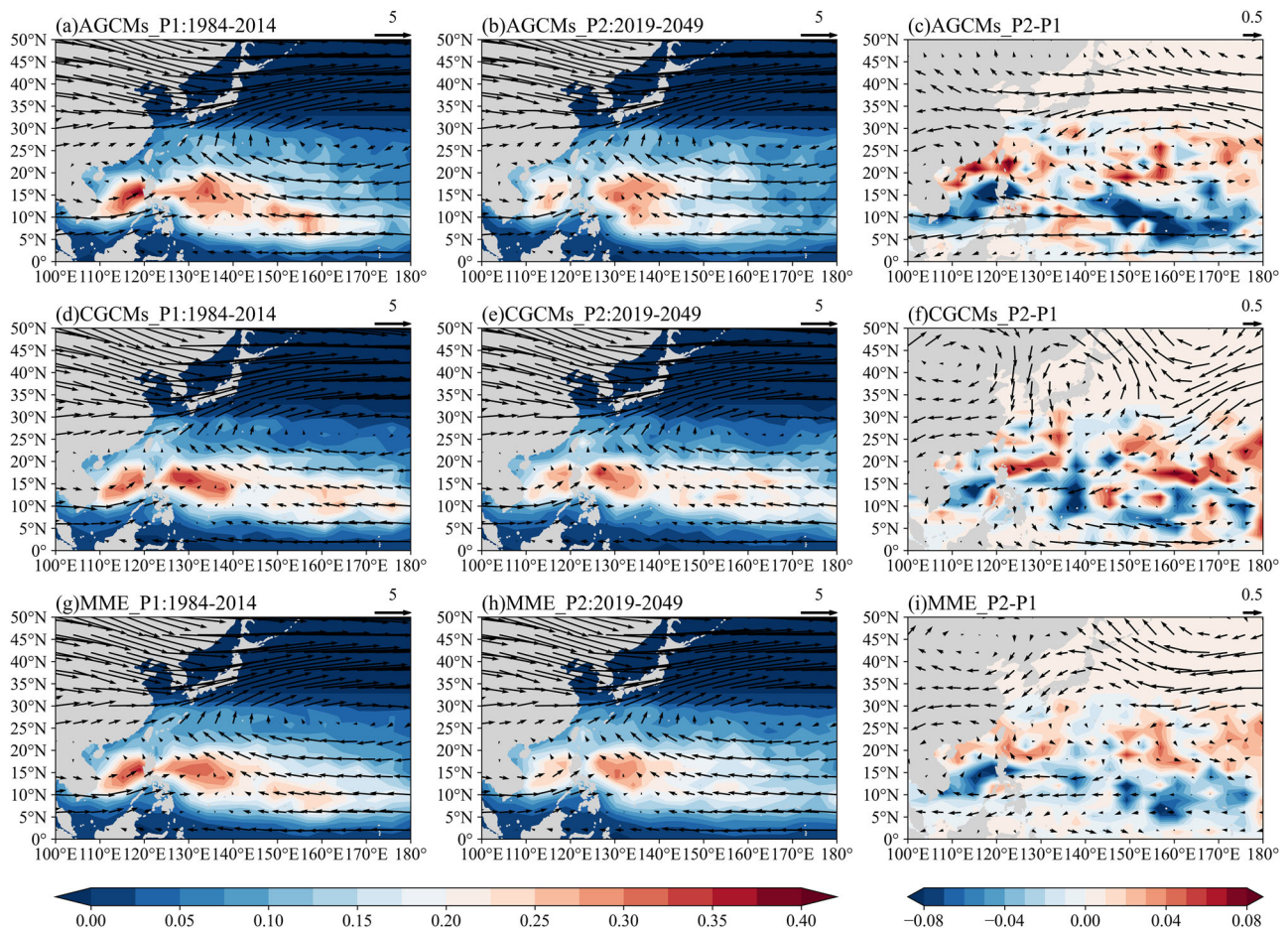


Fig. 5 | Long-term changes in TC genesis density and steering flow. Climatological distributions of TC genesis density and steering flow (m s^{-1}) (shown in vector) for a–c AGCMs, d–f CGCMs and g–i multi-model ensemble (MME) in the WNP averaged over P1 (1984–2014), P2 (2019–2049) and the differences between P1 vs. P2.

in the annual-mean φ_{LMI} , among which five/four models show statistically significant influences.

In the 101-year simulations, 75% models (15 out of 20) show the poleward migration of annual-mean φ_{LMI} with an MME rate of $0.067^\circ \text{decade}^{-1}$ (Fig. 4c, Supplementary Table 10, Supplementary Fig. 1). The fitted trends by the six factors are very close to the real trends with an MME rate of $0.068^\circ \text{decade}^{-1}$. Specifically, the genesis latitude contributes predominantly to the poleward migration of the annual-mean φ_{LMI} ; the MME contribution is $0.28^\circ \text{decade}^{-1}$ (Fig. 4d and Supplementary Table 10). Conversely, the trend of LMI is opposite to that of genesis latitude in most models (16 out of 20), and the MME contribution of LMI to the poleward migration is $-0.24^\circ \text{decade}^{-1}$. The meridional shift of MEHCAB contributes approximately $0.03^\circ \text{decade}^{-1}$. Whereas the contributions from the TC seasonality, the meridional steering flow and WNSPH strength are very small and negligible (Fig. 4d and Supplementary Table 10). Hence, the genesis latitude appears to be the leading influential factor on the annual-mean φ_{LMI} during the 101-year simulations. Compared to the 31-year simulation, the longer 101-year simulation shows a broad agreement among models with the genesis latitude moving poleward under global warming. This consensus among models leads to the broad agreement on the poleward migration of annual-mean φ_{LMI} .

Poleward shift of TC genesis and large-scale environmental changes

The poleward shifting genesis latitude may be mechanistically rooted in global warming-induced circulation adjustments^{50–52}. Under global warming, the WNSPH showed a poleward migration accompanied by the weakening of its southern branch, which reoriented the steering flow south

of the WNPSH northward (Fig. 5, Supplementary Figs. 2a, b). Thus, TCs formed in low latitudes tend to move northwestward or turn northward instead of moving westward directly (Fig. 5). The change of WNSPH is coupled with lower sea level pressure and enhanced ascending around $20^\circ\text{--}30^\circ\text{N}$ but higher sea level pressure and anomalous descending over $5^\circ\text{--}15^\circ\text{N}$ (Figs. 5 and 6). The anomalous descending strengthens the low-level trade winds and thus vertical wind shear, which may suppress the TC genesis near the equator (Supplementary Figs. 2b, c). North of 15°N , low-level vorticity exhibits a notable increase (Supplementary Fig. 2b), creating an environment conducive to TC genesis. Similar changes in these large-scale circulations have been reported both in observations (Supplementary Fig. 3) in recent decades and in numerical simulations under global warming^{53–58}. Synergistically, these changes help the northward shift of TC genesis and their northward propagation into the subtropics.

To further quantify how thermodynamic and dynamic environmental factors collectively modulate TC formation, we analyze changes in the dynamic genesis potential index (DGPI) that explicitly incorporates dynamic constraints (e.g., vertical velocity) beyond the thermodynamic framework¹² (see “Methods”). As shown in Fig. 7, the changes in DGPI reveal a poleward intensification pattern with a marked increase (decrease) north (south) of approximately 15°N (Fig. 7a, e, i), generally consistent with the poleward shift of TC genesis (Fig. 5c, f, i). We thus further define a pair of regions with opposite changes in DGPI to dissect the relative contributions of environmental factors on the poleward shift of TC genesis: area A ($4^\circ\text{N}\text{--}12^\circ\text{N}$, $150^\circ\text{E}\text{--}180^\circ\text{E}$) and area B ($14^\circ\text{N}\text{--}22^\circ\text{N}$, $158^\circ\text{E}\text{--}180^\circ\text{E}$) (Fig. 7a, e, i). It is apparent that 500 hPa vertical velocity is the dominant contributor across both regions, followed by 850 hPa absolute vorticity (Fig. 7b–d, f–h, j–l). The meridional gradient of 500 hPa zonal wind enhances the TC

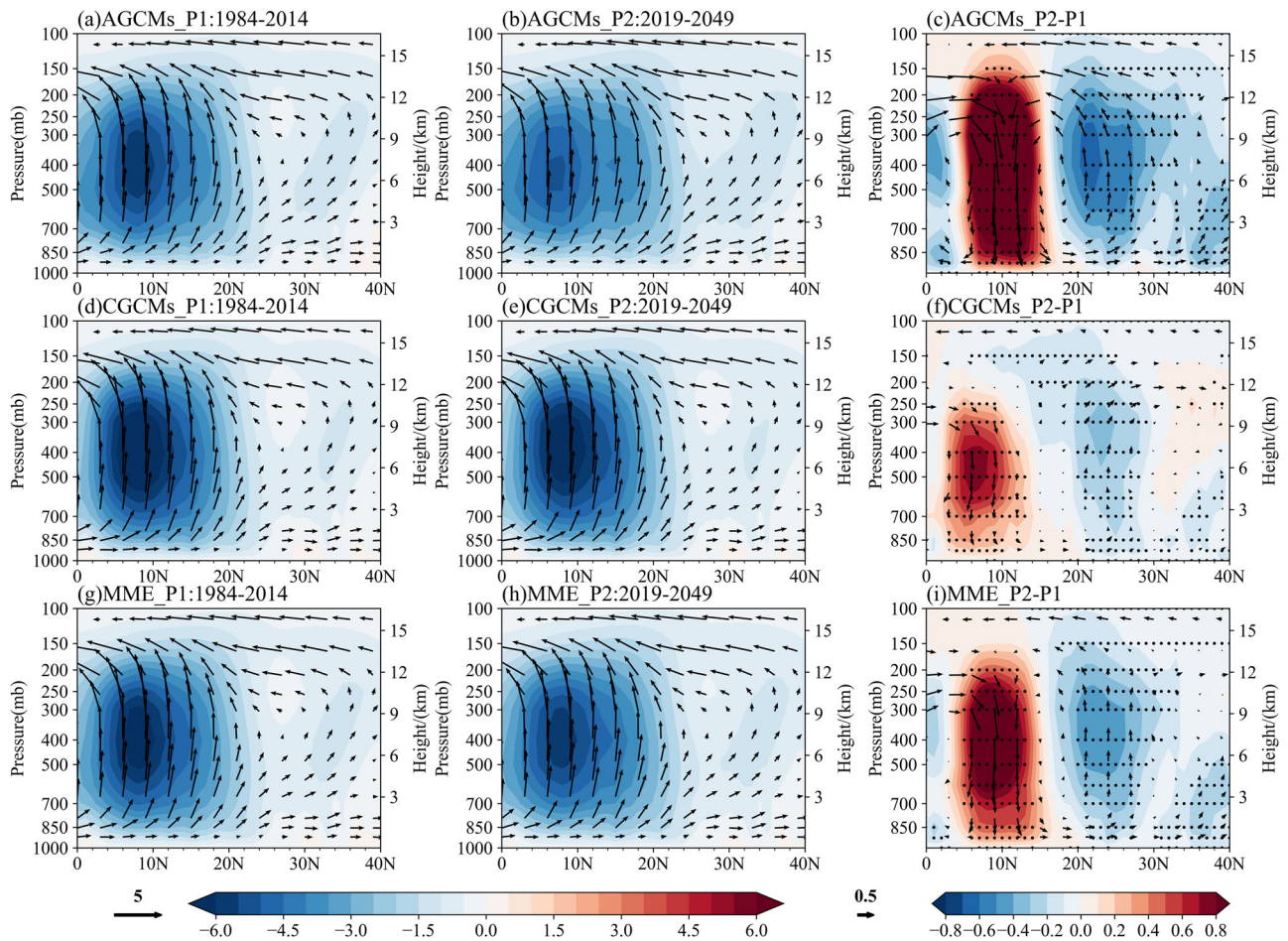


Fig. 6 | Meridional-vertical structure of the regional Hadley circulation. Meridional-vertical distribution of the longitudinally averaged divergent meridional wind (m s^{-1}) and vertical pressure velocity ($10^{-2} \text{ Pa s}^{-1}$) (shown in vector) for a–c AGCMs, d–f CGCMs, and g–i multi-model ensemble (MME) in the WNP

averaged over P1 (1984–2014), P2 (2019–2049) and the differences between P1 vs. P2. The shading over the same region shows the vertical pressure velocity. Negative (positive) values represent upward (downward) motion. Black dots denote values statistically significant at the 95% confidence level.

genesis in area B significantly, while the vertical wind shear term suppresses it in area A (Fig. 7j, k).

Discussion

We have demonstrated the dominant influence of genesis latitude on the long-term trend of annual-mean ϕ_{LMI} in the models participating in the PRIMAVERA project. In long-term simulations spanning one hundred years, most models exhibit a poleward migration of the genesis latitude under global warming, a point confirmed by early research^{10,16,49,59}, which leads to a corresponding poleward migration of the annual-mean ϕ_{LMI} . The poleward shifting genesis latitude may be mechanistically rooted in global warming-induced circulation adjustments. The northward migration of TC genesis density aligns with a northward shift of the ascending branch of the Hadley circulation under global warming. We note that although the MEHCAB itself contributes minimally to variations in the annual-mean ϕ_{LMI} in the regression analyses, it establishes the large-scale conditions that facilitate the northward shift of TC genesis, which indicates that the genesis latitude may reflect the integrated effects of global warming influencing the ϕ_{LMI} and raises the concern of multicollinearity in the regression equation of annual-mean ϕ_{LMI} . Even so, the multicollinearity concern is acceptable in the regression equation because inter-factor correlations are less than |0.6| (Supplementary Figs. 4 and 5) and the Variance Inflation Factors are predominantly less than 5, well below the conservative threshold of 10 (Methods, Supplementary Tables 7 and 13).

The regression equation here is estimated using the entire time period, which may lead to an overfitting problem. To address this concern, 5-fold

time series cross-validation is rigorously applied to both study periods (1984–2014 and 1950–2050). Cross-validated R^2 values (0.61–0.79) closely match in-sample R^2 (0.63–0.81), with RMSE deviations less than 15% from the reference trends (Data and Methods, Supplementary Tables 5, 6, 11, 12). Scatter plots further confirm cross-validation trends aligning tightly with the reference trends along the 1:1 line (Supplementary Figs. 6 and 7), demonstrating robust generalizability. In addition, to disentangle the respective roles of anthropogenic forcing and internal low-frequency climate modes, we apply a 3rd-order Butterworth low-pass filter (60-year cutoff) to the time series of annual-mean ϕ_{LMI} . The majority of models show consistent trends between filtered and unfiltered time series, with only minor variations in migration rates. This coherence demonstrates that anthropogenic forcing dominates the secular trend, while natural decadal variability does not fundamentally alter the forced response over a long time period.

To verify the conclusion that annual-mean ϕ_{LMI} and TC formation are likely to continue their poleward migration in the future, we conducted an independent numerical simulation by dynamically downscaling the outputs of the global climate model CESM2⁶⁰ using the regional climate model WRFv3.7^{61,62} in the domain from 100°E to 180°E and 0°N to 50°N. The downscaled outputs have a horizontal resolution of 20 km in the WNP and include the 1985–2014 historical run and the 2065–2094 future projection under the SSP2-4.5 and SSP5-8.5 scenarios, respectively (see “Methods”). Results show that the climatological latitude of TC genesis in the WNP is 5.4°N during 1985–2014 (historical period). Under SSP2-4.5, this latitude shifts northward to

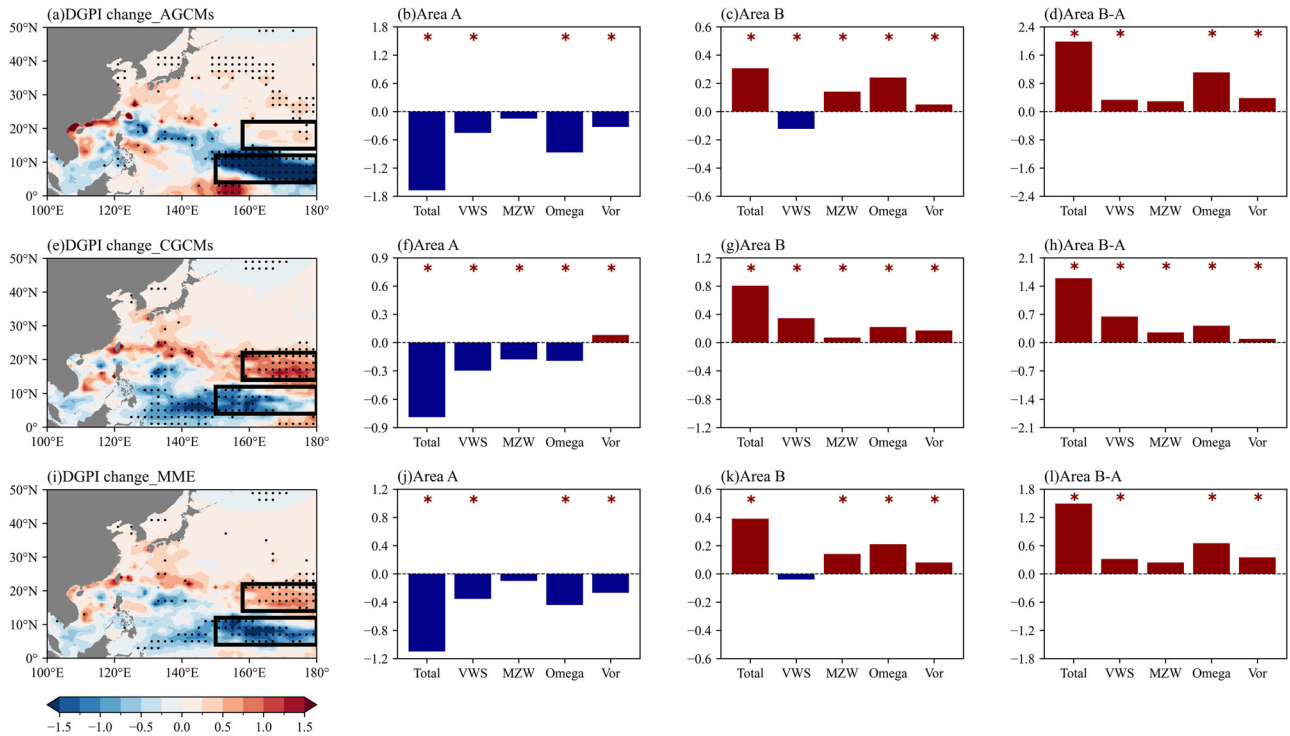


Fig. 7 | Future projections of the dynamic genesis potential index (DGPI) and relative contributions of its four terms. **a** Differences (P2-P1) in DGPI over the WNP between periods P1 (1984–2014) and P2 (2019–2049) for AGCMs and relative contributions of its four terms over **b** area A (4°N–12°N, 150°E–180°E), **c** area B (14°N–22°N, 158°E–180°E), and **d** the difference between A and B. Black dots and *

denote values statistically significant at the 95% confidence level. **e–h** as **a–d**, but for CGCMs. **i–l** as **a–d**, but for MME. VWS, MZW, Omega, and Vor represent the contributions from vertical wind shear, mid-level (500 hPa) zonal wind, vertical velocity, and low-level (850 hPa) absolute vorticity, respectively.

8.5°N during 2065–2094, representing a 3.1°N poleward migration; under SSP5–8.5, the genesis latitude reaches 8.9°N, a 3.5°N northward shift. Correspondingly, the climatological annual-mean ϕ_{LMI} is 10.5°N during 1985–2014 and shifts to 11.4°N (SSP2–4.5) and 12.2°N (SSP5–8.5) during 2065–2094, with poleward migration of 0.9°N and 1.7°N, respectively (Fig. 8). These results confirm that the latitudinal position of TC LMI tends to migrate northward under global warming due to the northward shift of TC genesis. Moreover, the extent of poleward migration is more pronounced under more severe warming scenarios. Notably, the concurrent poleward shifts of TC genesis and annual-mean ϕ_{LMI} under warming, as simulated by WRF, complement the conclusion from PRIMAVERA datasets, where the poleward migration of TC genesis is identified as a key driver of poleward migration of annual-mean ϕ_{LMI} in the future global warming. The consistency between the two analytical frameworks (PRIMAVERA-based global model analysis and WRF-driven regional downscaling) underscores the robustness of the linkage between TC genesis latitude shifts and ϕ_{LMI} migration under global warming. While this consistency supports our findings, several limitations of the PRIMAVERA dataset should be noted to contextualize our results. First, although the 101-year span of PRIMAVERA simulations (1950–2050) is sufficient to capture secular trends, this period may not fully resolve multidecadal variability. Second, the ten pairs of AGCMs vs. CGCMs may not be large enough to detect the significant impacts of air-sea coupling on the long-term trends of ϕ_{LMI} . Third, like most CMIP6 models, PRIMAVERA exhibits an El Niño-like tropical Pacific SST warming bias⁶³, which could slightly distort simulations of Hadley circulation shifts and thus TC activities. These limitations suggest future work with longer simulations, more model members, or pattern-conditioned SST constraints⁶³ would further strengthen our conclusions.

Upon the impacts of air-sea coupling on the long-term trend of simulated ϕ_{LMI} , the ten-paired AGCMs vs. CGCMs show different

distributions of the long-term trend, and the fitted trends reproduce well the differences (Figs. 3c and 4c). However, these differences are not statistically significant; twelve of the models show negative differences, while eight models exhibit positive differences during both the 1984–2014 and 1950–2050 periods (Figs. 3c and 4c; Supplementary Tables 4 and 10). The lack of significance may be attributed to the six influential factors that do not show statistically significant contributing differences between the AGCMs and the corresponding CGCMs (Figs. 3d and 4d; Supplementary Tables 2 and 8). Consequently, no statistically significant differences are detected between the AGCMs and their corresponding CGCMs. Hence, although air-sea coupling can influence the mean state of ϕ_{LMI} (Fig. 1), its impacts on the changes of ϕ_{LMI} under global warming seem insignificant. However, since the comparison is limited to only ten pairs of AGCMs vs. CGCMs, further analysis with more paired models is necessary to draw a definitive conclusion.

The present study focuses on the TCs in the WNP. It would be of interest to investigate the poleward migrations of TCs in other basins and the dominant influential factors in future work. Understanding regional differences and the consistency of poleward migration trends across different basins will provide a more comprehensive view of the impact of global warming on TC behavior worldwide.

Methods

Observational data

This study utilized the ERA5 reanalysis with a 0.25° resolution during 1982–2014⁴⁵. The observational TC data in the WNP (0°N–50°N, 100°E–180°E) during the same period were obtained from the International Best Track Archive for Climate Stewardship (IBTrACS v04r00). This dataset contains 6-hourly records of time, longitude, latitude, maximum sustained wind speed and central pressure of named tropical TCs. Our historical analyses focus on the 30-year period from 1984 to 2014, when the relatively reliable satellite observations are available.

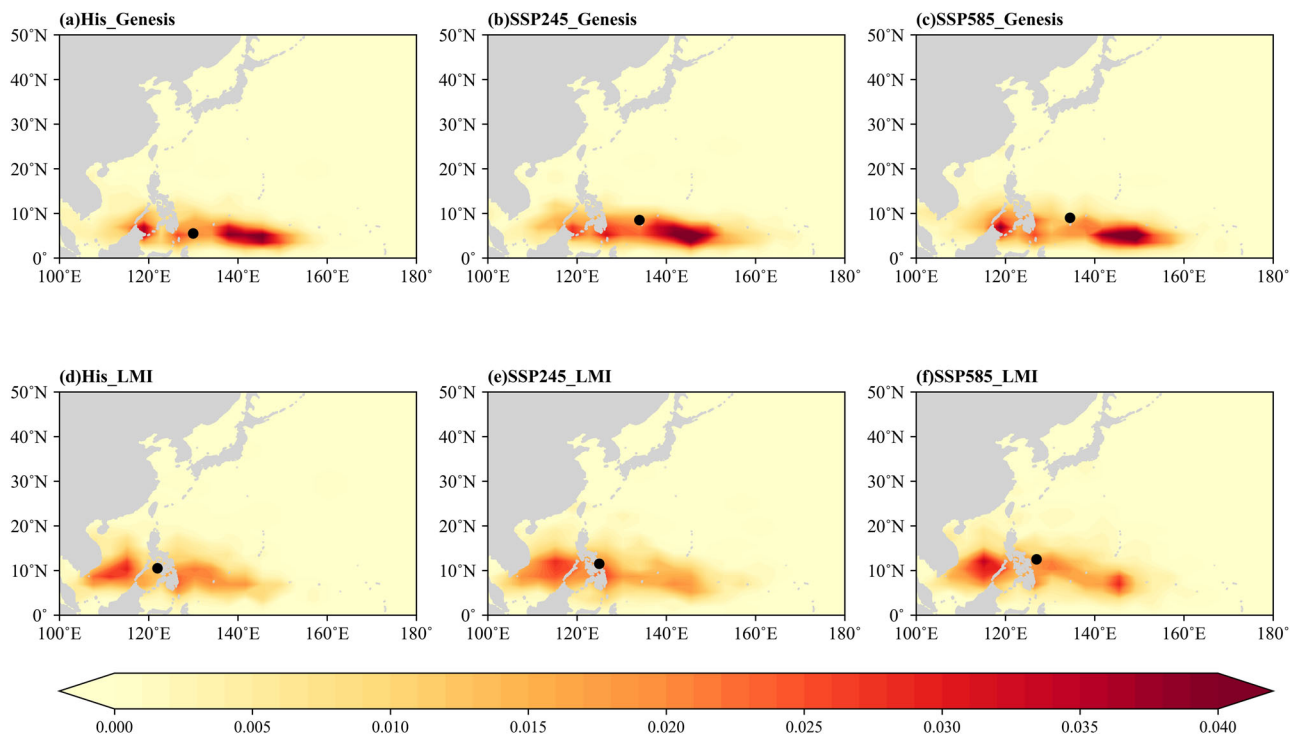


Fig. 8 | WRF-downscaled projections of TC genesis and LMI under climate change scenarios. Climatological distributions of climatological frequency of a–c TC genesis and d–f LMI based on a, c historical simulations spanning 1985–2014

and future projections spanning 2065–2094 under b, d the SSP2-4.5 and e, f SSP5-8.5 scenarios, respectively, in the WRFv3.7 driven by the outputs of CESM2. The dark dot in each plot represents the averaged position of all TCs.

CMIP6-HighResMIP data

The model outputs from the HighResMIP-PRIMAVERA project were used to evaluate model performance and analyze future projections. Although the project has six different modeling groups, the ECMWF-IFS⁶⁴ was excluded because it lacks a near-future projection. Therefore, five modeling groups were selected for this study: CMCC-CM2⁴⁰, CNRN-CM6-1⁴¹, HadGEM3-GC31⁴², EC-Earth3P⁴³ and MPI-ESM1.2⁴⁴. The experiments analyzed here were conducted at two different horizontal resolutions (Supplementary Table 1), a CMIP6-type low resolution (LR, ~100 km) and a higher resolution (HR, 25–50 km), by the atmosphere-only models (AGCMs) and the corresponding air-sea coupled versions (CGCMs). Each experiment was integrated from 1950 to 2050, covering the historical period (1950–2014) and a near-future projection (2015–2050)⁶⁵. For the AGCMs, the historical run was forced by observed SST and sea ice, and the future projection was forced by a blended variability from the observed SST and sea ice and the climate change signals obtained from the CMIP5 projections under the RCP8.5 scenario. For the CGCMs, the historical run considered the historic 1950–2014 anthropogenic forcing and the future projection was conducted under the SSP5-8.5 scenario⁶⁶. Readers are referred to Haarsma et al.⁶⁷ and Roberts et al.⁶⁸ for details of the experiment setups. In this study, if 75% of the models show the same-signed trend, the multi-model ensemble mean (MME) trend is regarded as statistically significant. Similarly, if 75% of pairs of AGCMs vs CGCMs or HR vs LR models show the same-signed differences, the MME differences are regarded as statistically significant.

Downscaling with the high-resolution WRF model

The Advanced Research WRFv3.7 climate model was configured to cover the domain from 100°E to 180°E and 0°N to 50°N, to simulate the weather and climate in East Asia and the WNP⁶². For these experiments, the horizontal resolution is 20 km with 33 vertical layers, with a domain-top pressure of 50 hPa. In our downscaling simulations, initial and lateral boundary conditions were interpolated from the CMIP6 CESM2 global circulation model outputs at a horizontal resolution of 1° × 1° with 6-h intervals. The CESM2 effectively replicates the atmospheric patterns

over the WNP and East Asia, showcasing its strong simulation capabilities⁶⁰. The historical downscaling simulations span from 1985 to 2014. The future projections last 30 years from 2065 to 2094 under the SSP2-4.5 and SSP5-8.5 scenarios, respectively. Considering the current limitations in computational resources for running cloud-resolving models, convection parameterization becomes a significant source of uncertainty in dynamical downscaling simulations of TC activity. To ensure simulation accuracy, an evaluation of parameterization schemes, especially the convective parameterization scheme, has been conducted (not shown). Finally, the following parameterization schemes were selected: the WRF Single-Moment 5-class (WSM5) cloud microphysics⁶⁹, Yonsei University (YSU) planetary boundary layer (PBL) scheme⁷⁰, Monin–Obukhov near-surface layer scheme⁷¹, the Noah land surface scheme⁷², the new Kain–Fritsch cumulus parameterization scheme⁷³ and the CAM radiation scheme⁷⁴ for longwave and shortwave radiations.

TC tracking and genesis

The TCs in the models of the HighResMIP-PRIMAVERA project were detected by the TC tracking algorithm “TRACK”⁷⁵. In this algorithm, the TC tracks are identified based on local maxima of the relative vorticity after the T63 resolution smoothing to reduce the impact of different original resolutions. Additionally, combine warm-core and lifetime criteria to ensure the identified storms have coherent vertical structure and a warm core. All TCs included in both observational datasets and model simulations are required to attain at least tropical storm (TS) intensity, defined as maximum sustained 10-m wind speed $V_{max} \geq 17 \text{ m s}^{-1}$ in the WNP.

The TCs in the WRFv3.7 were detected following the TC tracking algorithm developed by the Geophysical Fluid Dynamics Laboratory (GFDL, <https://www.gfdl.noaa.gov/tstorms/>), which has been widely used in TC research^{8,76}. For the 6-hourly model outputs, the primary variables (detection criteria) used for TC tracking include 850-hPa relative vorticity, 10-m maximum wind speed, and the center of the maximum temperature anomaly in the middle layer of the troposphere. Some modifications were

made to adapt the algorithm for these WRF simulations, and the TCs were extracted based on the following aspects:

1. Within a 300 km radius, track a local minimum in sea level pressure (SLP) as the TC center for that time step. The SLP must form a closed isobar, and the 850 hPa relative vorticity must exceed $5 \times 10^{-5} \text{ s}^{-1}$. Additionally, the minimum SLP must be at least 2 hPa lower than the SLP averaged over the surrounding 12×12 grid points.
2. The 10-m maximum wind speed within a 300-km radius from the SLP center must exceed 17 m s^{-1} .
3. The average wind speed at 850 hPa within a 300-km radius from the SLP center, over the entire TC life cycle, must not drop below 17 m s^{-1} at any time step and must remain above the average wind speed at 300 hPa.
4. The maximum value of the mid-level temperature anomaly (vertically averaged between 500 and 300 hPa) within a 300-km radius from the SLP center must exceed $1 \text{ }^\circ\text{C}$.
5. TCs must form in regions south of 30°N .

In each 6-hour simulation output, grid points that meet the above detection criteria are used for TC tracking. The duration of each TC life cycle must be at least 72 h. Each TC sample is examined to determine whether there is a cyclone within a 300 km radius for the next 6-hour time interval. If a detected cyclone satisfies the previous criteria, it is connected to the initial cyclone path to form a track.

We define TC genesis as the initial point of individual TC tracks. This approach avoids the need to define an intensity threshold of genesis or to account for intensity biases of simulated TCs. However, direct comparisons between observed and simulated TC genesis are complicated by differences in tracking methods. Observed TCs are typically tracked by human forecasters and researchers, with methods evolving over time, which differs fundamentally from the automated tracking used in numerical simulations. However, these discrepancies may not greatly influence our results, for this study focuses on the variations and long-term changes in the observations and simulations rather than on their climatologies.

Indices of φ_{LMI} and statistical analyses

In this study, the φ_{LMI} is defined as the latitude where the TC achieves its LMI in observations or numerical simulations, as in Kossin et al.⁵. The TC LMI is represented by the maximum 10-m wind speed. For TCs that achieve their LMI more than once, the φ_{LMI} at the first occurrence is considered. The annual-mean φ_{LMI} is calculated as the average of φ_{LMI} of all TCs in the WNP in a year. For the trend analysis, we estimate the trend using linear least-squares regression. The Pearson correlation coefficient is used to measure the correlation between the time series of two variables. The robustness of multiple linear regression usually depends on the choice of period. To enhance the reliability, we applied an improved Ordinary Least Squares (OLS) algorithm⁷⁷. Details of this OLS algorithm are provided in Supplementary Note 1. Following the methodologies of Kossin et al.⁶ and Li et al.⁷⁸, the influence of different factors on the long-term trend can be analyzed through multiple linear regression. Let L_n represent the annual-mean φ_{LMI} for year n in the WNP and $X_{i,n}$ be the i th influential factor in year n . Here, $n = 1, 2, \dots, 31$ for the 1984–2014 historical simulation, and $n = 1, 2, \dots, 101$ for the 1950–2050 simulation. The factors X_i considered in our study include TC genesis latitude, LMI, TC seasonality, MEHCAB, meridional steering flow and WNPSH strength. By applying the multiple linear regression method, the interannual variations in the annual-mean φ_{LMI} caused by the factors X_i can be expressed as: $L_n = \sum \theta_i X_{i,n} + \delta + \varepsilon_n$, where θ_i denotes the regression coefficient for the i th factor X_i , δ is the intercept and ε_n is the residual term. The long-term trend in L related to the six factors is equal to the sum of the product of θ_i (the regression coefficient of X_i) and the long-term trend in the i th influential factor X_i .

Indices of influential factors

1. Genesis latitude: Defined as the latitude of the initial point of individual TC tracks.

2. LMI: Defined as the maximum 10-m wind speed of TC.
3. TC seasonality: Defined as the ratio between the number of TC occurring from July to September and those from October to December each year.
4. Intensity of WNPSH subtropical high: Calculated as the sum of the product of the region area and the positive deviation of 500-hPa geopotential height from 5870 gpm in the region, as defined by He et al.⁷⁹.
5. Strength of meridional steering flow: Calculated as the three-dimensional average of the meridional velocity over the 300–850 hPa, $120^\circ\text{--}150^\circ\text{E}$ and $10^\circ\text{--}30^\circ\text{N}$. This region corresponds to the area of maximum meridional steering flow in the WNP.
6. MEHCAB: The Stokes streamfunction (ψ) reflects the strength and geometry of the Hadley circulation and is adopted to estimate the meridional extent of the Hadley circulation¹⁰. Assuming the non-divergent mean meridional circulation and mass conservation, ψ at a given latitude and pressure level can be calculated as:

$$\psi(\phi, p) = \frac{2\pi\alpha \cos \phi}{g} \int_0^p [v] dp, \quad (1)$$

where ϕ is the latitude, p is the pressure level, α is the earth radius and g is the acceleration due to gravity, the square bracket denotes the zonal average, and v is the meridional velocity. The three-dimensional average of ψ within 300–850 hPa, $120^\circ\text{--}150^\circ\text{E}$ and $0\text{--}10^\circ\text{N}$ is adopted to represent the meridional extent of the ascending branch of the Hadley circulation in the WNP.

Genesis potential index and dynamic genesis potential index

Vertical wind shear is calculated as the difference in horizontal wind vectors between 200 and 850 hPa. To capture dynamically driven TC formation, we employ the dynamic genesis potential index (DGPI) developed by Wang and Murakami^{80,81}, which explicitly incorporates dynamic constraints and further conduct a relative contribution analysis^{82–84}. DGPI can be calculated as follows:

$$DGPI = (2.0 + 1.0 \times V_s)^{-1.7} \left(5.5 - \frac{du_{500}}{dy} \right)^{2.3} (5 - 20 \times \omega_{500})^{3.4} (5.5 + |\zeta_{850} \times 10^5|)^{2.4} e^{-11.8} - 1.0, \quad (2)$$

where V_s is the vertical wind shear, u_{500} is the zonal wind at 500 hPa, ω_{500} is the vertical velocity at 500 hPa and ζ_{850} is the absolute vorticity at 850 hPa.

Cross-validation approach

To accurately evaluate and compare the performance of the multiple linear regression model, we employed a cross-validation approach to mitigate the risk of overfitting and ensure the model's robustness. Cross-validation enables the assessment of whether the relationships established between predictors and predictands hold consistently outside of the training data, thereby providing an indication of the model's generalizability to unseen data. The simplest and most commonly used cross-validation method is data splitting, where the data is partitioned into two sets—one for training (e.g., 80% of the data) and the other for validation (e.g., 20% of the data). However, this approach can introduce biases depending on the particular partitioning of the data. To address this limitation, we applied K-fold cross-validation, which provides a more rigorous validation by using multiple combinations of training and test datasets. In this method, the available data are divided into K non-overlapping subsets, or “folds,” with each fold containing approximately n/K elements. For each fold, the model is trained on $K-1$ folds and tested on the remaining fold. This process is repeated K times, each time with a different fold as the test set. The results from these K iterations are then aggregated into a single validation series that spans the entire analysis period^{85,86}. This approach not only provides a more robust

estimate of the model's performance but also allows for the analysis of variability across different validation periods.

In this study, we employed a 5-fold cross-validation approach using two distinct time periods: 1984–2014 and 1950–2050. For the 1984–2014 period, the data were divided into five 5-year intervals: 1990–1994, 1995–1999, 2000–2004, 2005–2009, and 2010–2014. Similarly, for the 1950–2050 period, the data were partitioned into five intervals: 1971–1986, 1987–2002, 2003–2018, 2019–2034, and 2035–2050. The choice of five folds strikes a balance between having sufficiently long validation periods and retaining enough data for model training. To further assess the model's performance, we utilized scatter plots to visualize the relationship between the reference (observed and modeled) trends and the trends derived from the 5-fold cross-validation process (Supplementary Figs. 6 and 7). In these plots, the black line represents the 1:1 line, indicating perfect correlation between the reference and cross-validation trends. Ideally, a good model would show data points closely aligned along this 1:1 line. The red and blue lines represent the 1:2 and 2:1 lines, respectively, and serve as references to highlight deviations from perfect agreement. A trend closer to the 1:1 line suggests better model performance, as it indicates that the cross-validation predictions closely match the observed data.

Variance inflation factor (VIF)

Multicollinearity occurs when two or more predictor variables in a regression model are highly correlated, leading to unreliable coefficient estimates and inflated standard errors. The VIF is a statistical measure used to quantify the severity of multicollinearity in a regression analysis⁸⁷. The VIF for a predictor variable X_j is calculated as:

$$VIF_j = \frac{1}{1 - X_j^2}, \text{ Limits are : } 1 \leq VIF_j \leq \infty \text{ and } 0 \leq X_j^2 \leq 1 \quad (3)$$

VIF = 1: No multicollinearity.

1 < VIF < 5: Moderate correlation (usually acceptable).

VIF ≥ 5 (or 10): High multicollinearity (may require corrective action, such as removing variables or using regularization techniques). If VIF ≤ 10, then it may be concluded that there is no serious case of multicollinearity.

Data availability

The ERA5 climate reanalysis was generated and distributed by the Copernicus Climate Data Store (<https://cds.climate.copernicus.eu#!/home>). The TC best-track data used in this study were IBTrACS (v04r00) data, retrieved from the NOAA National Centers for Environmental Information (<https://www.ncei.noaa.gov/products/international-best-track-archive>). The CMIP6-HighResMIP data are openly available at <https://data.ceda.ac.uk/badc/cmip6/data/CMIP6/HighResMIP>. The tropical storm tracks calculated by the TRACK algorithm can be downloaded at <http://catalogue.ceda.ac.uk/uuid/0b42715a7a804290afa9b7e31f5d7753>. The variables in the CMIP6-HighResMIP models are available at <https://data.ceda.ac.uk/badc/cmip6/data/CMIP6/HighResMIP>.

Code availability

The main scripts for data processing and plotting are available at GitHub (<https://github.com/LiMY-at/poleshift>). Other source codes are available from Mingyu Li (lm443282765@gmail.com) upon request.

Received: 13 September 2024; Accepted: 6 August 2025;

Published online: 22 August 2025

References

1. Maue, R. N. Recent historically low global tropical cyclone activity. *Geophys. Res. Lett.* **38**, 673–684 (2001).
2. Xu, P. et al. Structural changes in the Pacific–Japan pattern in the late 1990s. *J. Clim.* **32**, 607–621 (2019).
3. Horinouchi, T. et al. Moisture supply, jet, and silk-road wave train associated with the prolonged heavy rainfall in Kyushu, Japan in early July 2020. *Sci. Online Lett. Atmos.* **17**, 1–8 (2021).
4. Kossin, J. P., Olander, T. L. & Knapp, K. R. Trend analysis with a new global record of tropical cyclone intensity. *J. Clim.* **26**, 9960–9976 (2013).
5. Kossin, J. P., Emanuel, K. A. & Vecchi, G. A. The poleward migration of the location of tropical cyclone maximum intensity. *Nature* **509**, 349–352 (2014).
6. Kossin, J. P., Emanuel, K. A. & Camargo, S. J. Past and projected changes in western North Pacific tropical cyclone exposure. *J. Clim.* **29**, 5725–5739 (2016).
7. Yokoi, S. & Takayabu, Y. N. Multi-model projection of global warming impact on tropical cyclone genesis frequency over the western North Pacific. *J. Meteorol. Soc. Jpn.* **87**, 525–538 (2009).
8. Murakami, H. et al. Future changes in tropical cyclone activity projected by the new high-resolution MRI-AGCM. *J. Clim.* **25**, 3237–3260 (2012).
9. Park, D. S. R., Ho, C. H. & Kim, J. H. Growing threat of intense tropical cyclones to East Asia over the period 1977–2010. *Environ. Res. Lett.* **9**, 014008 (2014).
10. Sharmila, S. & Walsh, K. Recent poleward shift of tropical cyclone formation linked to Hadley cell expansion. *Nat. Clim. Change* **8**, 730–736 (2018).
11. Zhan, R. & Wang, Y. Weak tropical cyclones dominate the poleward migration of the annual mean location of lifetime maximum intensity of Northwest Pacific tropical cyclones since 1980. *J. Clim.* **30**, 6873–6882 (2017).
12. Daloz, A. S. & Camargo, S. J. Is the poleward migration of tropical cyclone maximum intensity associated with a poleward migration of tropical cyclone genesis?. *Clim. Dyn.* **50**, 705–715 (2018).
13. Feng, X. B., Klingaman, N. P. & Hodges, K. L. Poleward migration of western North Pacific tropical cyclones related to changes in cyclone seasonality. *Nat. Clim.* **12**, 1–11 (2021).
14. Song, J. & Klotzbach, P. J. What has controlled the poleward migration of annual averaged location of tropical cyclone lifetime maximum intensity over the western North Pacific since 1961?. *Geophys. Res. Lett.* **45**, 1148–1156 (2018).
15. Wang, R. & Wu, L. Influence of track changes on the poleward shift of LMI location of western North Pacific tropical cyclones. *J. Clim.* **32**, 8437–8445 (2019).
16. Zhao, H. et al. Interannual and interdecadal drivers of meridional migration of western North Pacific tropical cyclone lifetime maximum intensity location. *J. Clim.* **35**, 2709–2722 (2022).
17. Feng, X. B. Translation speed slowdown and poleward migration of western North Pacific tropical cyclones. *npj Clim. Atmos. Sci.* **7**, 196 (2024).
18. Sun, Y. et al. A recent reversal in the poleward shift of western North Pacific tropical cyclones. *Geophys. Res. Lett.* **45**, 9944–9952 (2018).
19. Guo, Y. P. & Tan, Z. M. Influence of track change on the inconsistent poleward migration of typhoon activity. *J. Geophys. Res. Atmos.* **127**, e2022JD036640 (2022).
20. Lin, J., Lee, C. Y., Camargo, S. J. & Sobel, A. Poleward migration of the latitude of maximum tropical cyclone intensity—forced or natural? *J. Clim.* **37**, 5453–5463 (2024).
21. Dong, B. & Dai, A. The influence of the interdecadal Pacific oscillation on temperature and precipitation over the globe. *Clim. Dyn.* **45**, 2667–2681 (2015).
22. Li, W., Li, L. & Deng, Y. Impact of the interdecadal Pacific oscillation on tropical cyclone activity in the North Atlantic and eastern North Pacific. *Sci. Rep.* **5**, 12358 (2015).
23. Zhao, J. et al. Distinct modulations of northwest Pacific tropical cyclone precipitation by Atlantic multidecadal oscillation and interdecadal Pacific oscillation. *Geophys. Res. Lett.* **51**, e2023GL107749 (2024).

24. Knight, J. R., Folland, C. K. & Scaife, A. A. Climate impacts of the Atlantic multidecadal oscillation. *Geophys. Res. Lett.* **33**, L17706 (2006).
25. Klotzbach, P. J. The influence of El Niño–Southern Oscillation and the Atlantic multidecadal oscillation on Caribbean tropical cyclone activity. *J. Clim.* **24**, 721–731 (2011).
26. Song, K. et al. Influence of the Atlantic multidecadal oscillation on the rapid intensification magnitude of tropical cyclones over the western North Pacific. *J. Clim.* **37**, 689–730 (2024).
27. Zhao, J., Zhan, R., Wang, Y. & Xu, H. Contribution of the interdecadal Pacific oscillation to the recent abrupt decrease in tropical cyclone genesis frequency over the western North Pacific since 1998. *J. Clim.* **31**, 8211–8224 (2018).
28. Tennille, S. A. & Ellis, K. N. Spatial and temporal trends in the location of the lifetime maximum intensity of tropical cyclones. *Atmosphere* **8**, 198 (2017).
29. Manganello, J. V. et al. Tropical cyclone climatology in a 10-km global atmospheric GCM: toward weather-resolving climate modeling. *J. Clim.* **25**, 3867–3893 (2012).
30. Strachan, J. et al. Investigating global tropical cyclone activity with a hierarchy of AGCMs: the role of model resolution. *J. Clim.* **26**, 133–152 (2013).
31. Camargo, S. J. Global and regional aspects of tropical cyclone activity in the CMIP5 models. *J. Clim.* **26**, 9880–9902 (2013).
32. Moon, Y. et al. Azimuthally averaged wind and thermodynamic structures of tropical cyclones in global climate models and their sensitivity to horizontal resolution. *J. Clim.* **33**, 1575–1595 (2019).
33. Moon, I. J., Kim, S. H., Klotzbach, P. & Chan, J. C. L. Roles of interbasin frequency changes in the poleward shifts of the maximum intensity location of tropical cyclones. *Environ. Res. Lett.* **10**, 104004 (2015).
34. Zhang, W. et al. Tropical cyclone precipitation in the HighResMIP atmosphere-only experiments of the PRIMAVERA Project. *Clim. Dyn.* **57**, 253–273 (2021).
35. Huang, H., Patricola, C. M. & Collins, W. D. The influence of ocean coupling on simulated and projected tropical cyclone precipitation in the HighResMIP-PRIMAVERA simulations. *Geophys. Res. Lett.* **48**, e2021GL094801 (2021).
36. Liu, J. C., Yuan, C. X. & Luo, J. J. Impacts of model resolution on responses of western North Pacific tropical cyclones to ENSO in the HighResMIP-PRIMAVERA ensemble. *Front. Earth Sci.* **11**, 1169885 (2023).
37. Lin, J., Lee, C. Y., Camargo, S. J. & Sobel, A. Poleward migration of the latitude of maximum tropical cyclone intensity forced or natural? *J. Clim.* **37**, 5453–5463 (2024).
38. Haarsma, R. et al. HighResMIP versions of EC-Earth: EC-Earth3P and EC-Earth3P-HR-description, model computational performance and basic validation. *Geosci. Model Dev. Discuss.* **2020**, 1–37 (2020).
39. Roberts, M. J. et al. Impact of model resolution on tropical cyclone simulation using the HighResMIP-PRIMAVERA multi-model ensemble. *J. Clim.* **33**, 2557–2583 (2020).
40. Cherchi, A. et al. Global mean climate and main patterns of variability in the CMCC-CM2 coupled model. *J. Clim.* **11**, 185–209 (2019).
41. Voldoire, A. et al. Evaluation of CMIP6 DECK experiments with CNRM-CM6-1. *J. Adv. Model. Earth Syst.* **11**, 2177–2213 (2019).
42. Roberts, M. J. et al. Description of the resolution hierarchy of the global coupled HadGEM3-GC3.1 model as used in CMIP6 HighResMIP experiments. *Geosci. Model Dev.* **12**, 4999–5028 (2019).
43. Haarsma, R. J. et al. High resolution model intercomparison project (HighResMIP v1. 0) for CMIP6. *Geosci. Model Dev.* **9**, 4185–4208 (2016).
44. Gutjahr, O. et al. Max Planck Institute Earth System Model (MPI-ESM1. 2) for the high-resolution model intercomparison project (HighResMIP). *Geosci. Model Dev.* **12**, 3241–3281 (2019).
45. Hersbach, H. et al. The ERA5 global reanalysis. *Q. J. R. Meteorol. Soc.* **146**, 1999–2049 (2020).
46. Li, H. et al. Subtropical high affects interdecadal variability of tropical cyclone genesis in the South China Sea. *J. Geophys. Res. Atmos.* **124**, 6379–6392 (2019).
47. Li, H. et al. Unusual tropical cyclone tracks under the influence of upper-tropospheric cold low. *Mon. Weather Rev.* **152**, 39–58 (2024).
48. Shimada, U. Variability of environmental conditions for tropical cyclone rapid intensification in the western North Pacific. *J. Clim.* **35**, 4437–4454 (2022).
49. Walsh, K. J. E. et al. Tropical cyclones and climate change. *Wiley Interdiscip. Rev. Clim. Change* **7**, 65–89 (2016).
50. Ose, T., Song, Y. & Kitoh, A. Sea surface temperature in the South China Sea an index for the Asian monsoon and ENSO system. *J. Meteorol. Soc. Jpn.* **75**, 1091–1107 (1997).
51. Ose, T. Future precipitation changes during summer in East Asia and model dependence in high-resolution MRI-AGCM experiments. *Hydrol. Res. Lett.* **11**, 168–174 (2017).
52. Ose, T. Characteristics of future changes in summertime East Asian monthly precipitation in MRI-AGCM global warming experiments. *J. Meteorol. Soc. Jpn.* **97**, 317–335 (2019).
53. Ose, T., Takaya, Y., Maeda, S. & Nakaegawa, T. Resolution of summertime East Asian pressure pattern and southerly monsoon wind in CMIP5 multi-model future projections. *J. Meteorol. Soc. Jpn.* **98**, 927–944 (2020).
54. Ose, T., Endo, H., Takaya, Y., Maeda, S. & Nakaegawa, T. Robust and uncertain sea-level pressure patterns over summertime East Asia in the CMIP6 multi-model future projections. *J. Meteorol. Soc. Jpn.* **100**, 631–645 (2022).
55. Ose, T., Endo, H. & Nakaegawa, T. Emergence of future sea-level pressure patterns in recent summertime East Asia. *J. Meteorol. Soc. Jpn.* **102**, 265–283 (2024).
56. Boisséson, E. D. et al. How robust is the recent strengthening of the tropical Pacific trade winds? *Geophys. Res. Lett.* **41**, 4398–4405 (2014).
57. Ma, S. & Zhou, T. Robust strengthening and westward shift of the tropical Pacific Walker circulation during 1979–2012: A comparison of 7 sets of reanalysis data and 26 CMIP5 models. *J. Clim.* **29**, 3097–3118 (2016).
58. Li, Y. et al. Long-term trend of the tropical Pacific trade winds under global warming and its causes. *J. Geophys. Res. Oceans* **124**, 2626–2640 (2019).
59. Zhao, M. & Held, I. M. TC-permitting GCM simulations of hurricane frequency response to sea surface temperature anomalies projected for the late-twenty-first century. *J. Clim.* **25**, 2995–3009 (2012).
60. Danabasoglu, G. et al. The Community Earth System Model Version 2 (CESM2). *J. Adv. Model. Earth Syst.* **129**, 569–585 (2020).
61. Laprise, R. The Euler equations of motion with hydrostatic pressure as an independent variable. *Mon. Weather Rev.* **129**, 569–585 (1992).
62. Giorgi, F., Jones, C. & Asrar, G. R. Addressing climate information needs at the regional level: the CORDEX framework. *WMO Bull.* **58**, 175 (2009).
63. Wang, Y., Satoh, M., Zhan, J., Zhao, J. & Xie, S. P. Tropical sea surface warming patterns and tropical cyclone activity: a review. *Adv. Atmos. Sci.* **42**, 1996–2017 (2025).
64. Roberts, C. D. et al. ECMWF ECMWF-IFS-HR model output prepared for CMIP6 HighResMIP. *Earth Syst. Grid Fed.* <https://doi.org/10.22033/ESGF/CMIP6.2461> (2017).
65. Tang, Y., Huangfu, J., Huang, R. & Chen, W. Simulation and projection of tropical cyclone activities over the western North Pacific by CMIP6 HighResMIP. *J. Clim.* **35**, 7771–7794 (2022).
66. Li, Z. & Zhou, W. Poleward migration of tropical cyclones over the western North Pacific in the CMIP6-HighResMIP models constrained by observations. *npj Clim. Atmos. Sci.* **7**, 161 (2024).

67. Haarsma, R. J. et al. High resolution model intercomparison project (HighResMIP v1.0) for CMIP6. *Geosci. Model Dev.* **9**, 4185–4208 (2016).
68. Roberts, M. J. et al. Projected future changes in tropical cyclones using the CMIP6 HighResMIP multi-model ensemble. *Geophys. Res. Lett.* **47**, 1–12 (2020).
69. Hong, S. Y., Dudhia, J. & Chen, S. H. A revised approach to ice microphysical processes for the bulk parameterization of clouds and precipitation. *Mon. Weather Rev.* **132**, 103–120 (2004).
70. Hong, S. Y., Noh, Y. & Dudhia, J. A new vertical diffusion package with an explicit treatment of entrainment processes. *Mon. Weather Rev.* **134**, 2318–2341 (2006).
71. Paulson, C. A. The mathematical representation of wind speed and temperature profiles in the unstable atmospheric surface layer. *J. Appl. Meteorol.* **9**, 857–861 (1970).
72. Chen, F. & Dudhia, J. Coupling an advanced land surface–hydrology model with the Penn State–NCAR MM5 modeling system. Part I: model implementation and sensitivity. *Mon. Weather Rev.* **129**, 569–585 (2001).
73. Kain, J. S. The Kain–Fritsch convective parameterization: an update. *J. Appl. Meteorol.* **43**, 170–181 (2004).
74. Collins, W. D. et al. Description of the NCAR community atmosphere model (CAM 3.0). *NCAR Tech. Note NCAR/TN-464+ Str.* **226**, 1326–1334 (2004).
75. Hodges, K., Cobb, A. & Vidale, P. L. How well are tropical cyclones represented in reanalysis datasets?. *J. Clim.* **30**, 5243–5264 (2017).
76. Zhao, J. et al. Untangling impacts of global warming and Interdecadal Pacific Oscillation on long-term variability of North Pacific tropical cyclone track density. *Sci. Adv.* **6**, eaba6813 (2020).
77. Lian, T. Uncertainty in detecting trend: a new criterion and its applications to global SST. *Clim. Dyn.* **49**, 2881–2893 (2017).
78. Li, Y. et al. Recent increases in tropical cyclone rapid intensification events in global offshore regions. *Nat. Commun.* **14**, 5167 (2023).
79. He, J. H., Zhou, B., Wen, M. & Li, F. Vertical circulation structure, interannual variation features and variation mechanism of western Pacific subtropical high. *Adv. Atmos. Sci.* **18**, 497–510 (2001).
80. Emanuel, K. A. & Nolan, D. S. Tropical cyclone activity and the global climate system. *26th. Conf. Hurric. Trop. Meteorol.* **10A.2**, 240–241 (2004).
81. Wang, B. & Murakami, H. Dynamic genesis potential index for diagnosing present-day and future global tropical cyclone genesis. *Environ. Res. Lett.* **15**, 114008 (2020).
82. Camargo, S. J. et al. Characteristics of model tropical cyclone climatology and the large-scale environment. *J. Clim.* **33**, 4463–4487 (2020).
83. Zhao, H. et al. On the relationship between eastern China aerosols and western North Pacific tropical cyclone activity. *Atmos. Res.* **284**, 106604 (2023).
84. Jian, D. et al. Projected poleward migration of western North Pacific tropical cyclone genesis. *Geophys. Res. Lett.* **51**, e2024GL110031 (2024).
85. Gutiérrez, J. M. et al. Reassessing statistical downscaling techniques for their robust application under climate change conditions. *J. Clim.* **26**, 171–188 (2013).
86. Gutiérrez, J. M. et al. An intercomparison of a large ensemble of statistical downscaling methods over Europe: results from the VALUE perfect predictor cross-validation experiment. *Int. J. Climatol.* **39**, 3750–3785 (2019).
87. Fox, J. & Monette, G. Generalized collinearity diagnostics. *J. Am. Stat. Assoc.* **87**, 178–183 (1992).

Acknowledgements

This study is financially supported by the National Natural Science Foundation of China (42088101), National Key Research and Development Program of China (2022YFF0801702) and the Postgraduate Research and Practice Innovation Program of Jiangsu Province (KYCX24_1423). The analyses were conducted in the super computer in the High Performance Computing Center of Nanjing University of Information Science and Technology.

Author contributions

M.-Y.L. and C.-X.Y. conceived the study. M.-Y.L. performed the analyses and wrote the manuscript. C.-X.Y. helped edit the manuscript and refine the results. J.-W.Z. and Q.-Q.L. discussed the results and edited the paper. All authors contributed to interpreting the results and improving this paper.

Competing interests

The authors declare no competing interests.

Additional information

Supplementary information The online version contains supplementary material available at <https://doi.org/10.1038/s41612-025-01194-7>.

Correspondence and requests for materials should be addressed to Chaoxia Yuan.

Reprints and permissions information is available at <http://www.nature.com/reprints>

Publisher's note Springer Nature remains neutral with regard to jurisdictional claims in published maps and institutional affiliations.

Open Access This article is licensed under a Creative Commons Attribution-NonCommercial-NoDerivatives 4.0 International License, which permits any non-commercial use, sharing, distribution and reproduction in any medium or format, as long as you give appropriate credit to the original author(s) and the source, provide a link to the Creative Commons licence, and indicate if you modified the licensed material. You do not have permission under this licence to share adapted material derived from this article or parts of it. The images or other third party material in this article are included in the article's Creative Commons licence, unless indicated otherwise in a credit line to the material. If material is not included in the article's Creative Commons licence and your intended use is not permitted by statutory regulation or exceeds the permitted use, you will need to obtain permission directly from the copyright holder. To view a copy of this licence, visit <http://creativecommons.org/licenses/by-nc-nd/4.0/>.

© The Author(s) 2025